

## Coordinated Interplanetary Scintillation Observations in Japan and Russia for Coronal Mass Ejection Events in Early September 2017

Munetoshi Tokumaru <sup>1</sup>  · Ken'ichi Fujiki<sup>1</sup> ·  
Kazumasa Iwai<sup>1</sup> · Sergey Tyul'bashev<sup>2</sup> ·  
Igor Chashei<sup>2</sup>

© Springer ●●●

**Abstract** Interplanetary (IP) shocks travelling between the Sun and the Earth's orbit were clearly detected in interplanetary scintillation (IPS) observations made at Toyokawa (Japan) and Pushchino (Russia), in association with two halo coronal mass ejections (CMEs) that occurred on 04 and 06 September 2017. Since the observation times at Toyokawa and Pushchino differ by about six hours, a combined analysis of the IPS data obtained at these sites enabled high-cadence tracking of the IP shock for one of the CME events. The plane-of-sky locations where the IP disturbances were observed at Toyokawa were generally consistent with those at Pushchino. The propagation speeds of IP shocks inferred from IPS observations were higher than the average speeds derived from the occurrence time of IP shocks at Earth. This difference was ascribed to the deceleration of the CME-driven shocks during propagation. The East–West asymmetry of the propagation speed of IP shocks was also revealed from IPS observations. Solar-wind disturbances moving at a speed significantly slower than the average speed of the IP shock were identified from the IPS observations of the 06 September 2017 halo CME event. A wide longitudinal extent of these slow disturbances was suggested by the fact they were observed not only west but also east of the Sun; *i.e.* the opposite side to the flare/CME site. The origin of the slow disturbances is considered to represent either wing portions of the highly warped IP shock or the post-shock dense materials.

**Keywords:** Coronal Mass Ejection, Interplanetary Scintillation, Solar Wind, Space Weather

---

✉ M. Tokumaru  
tokumaru@isee.nagoya-u.ac.jp

<sup>1</sup> Institute for Space-Earth Environmental Research, Nagoya University, Nagoya, Japan

<sup>2</sup> Lebedev Physical Institute, Pushchino Radio Astronomy Observatory, Moscow region, Russia

## 1. Introduction

Interplanetary scintillation (IPS) from a compact radio source serves as an effective tool for remote sensing of the solar wind (Hewish, Scott, and Wills, 1964), particularly a transient stream associated with a coronal mass ejection (CME). For weak scattering, the strength of IPS is approximately proportional to the integrated level of solar-wind (electron) density fluctuations  $[\Delta N_e]$ . When the highly turbulent plasma associated with a CME intersects the line of sight (LOS) to a radio source, the IPS strength abruptly increases above its mean level which slowly varies due to the quasi-stationary structures of the ambient solar wind. Plotting the locations of the enhanced IPS on the plane of the sky yields a distribution map of CMEs in the solar wind. Such IPS mapping observations were used to study the global properties and propagation dynamics of CMEs travelling between the Sun and the Earth's orbit (*e.g.* Vlasov, 1979; Shishov, Vlasov and Kojima, 1997; Tokumaru *et al.*, 2000; Manoharan *et al.*, 2001; Tokumaru *et al.*, 2003, 2005; Manoharan, 2006; Tokumaru *et al.*, 2006, 2007; Iju, Tokumaru, and Fujiki, 2013, 2014; Chashei *et al.*, 2015, 2016; Shishov *et al.*, 2016; Chashei *et al.*, 2018). We note that the interplanetary counterpart of a fast CME is composed of the high-density plasma at the CME-driven shock and the rarefied plasma following it in most cases. Therefore, the enhancements of the IPS strength are considered to represent the shocked plasma, since  $\Delta N_e$  is roughly proportional to the bulk (electron) density  $[N_e]$  (Armstrong and Coles, 1978; Coles *et al.*, 1978; Lynch, Coles, and Sheeley, 2002). A close correlation between abrupt enhancements in the IPS strength and the compression regions at the leading edges of transient high-speed streams was demonstrated from the comparison study using Cambridge IPS and in-situ observations (Moore and Harrison, 1994).

The spatial resolution of the IPS mapping depends on the number of LOS available for IPS observations on a given day, and can be improved by using a high-sensitivity large-aperture radio telescope. However, the temporal cadence for IPS mapping is not easy to improve, since observation time is greatly limited by the characteristics of the system. IPS observations of a given source are often performed at around the meridian transit time, depending on the specification of the system. Furthermore the inner solar wind cannot be observed at a ground-based station at nighttime. This limited temporal cadence sometimes becomes a serious problem for fast moving CMEs. The CME feature revealed by the IPS mapping is significantly affected by rapid motion. Fast CMEs may not be detected by IPS observations at some sites, if they have sufficiently high speeds. The temporal cadence of IPS mapping can be improved by combining IPS observations at different longitudes. A global network composing existing IPS systems called the world-wide IPS stations (WIPSS) has been proposed to optimize the utility of IPS observations for the study of CMEs and space weather (Bisi *et al.*, 2016).

This article presents our combined analysis of IPS observations performed at Pushchino, Russia and Toyokawa, Japan for halo CME events in early September 2017. IPS observations were conducted daily at both stations during the event period, and interplanetary (IP) disturbances associated with halo CMEs were

clearly detected from those observations (Pushchino IPS observations during this period were presented by Chashei *et al.*, 2018). The combined analysis of these IPS observations provided the improved temporal cadence of IPS mapping that enabled detailed discussion of the propagation of CMEs in the solar wind. The outline of this article is as follows: Section 2 presents the IPS observations at Toyokawa and Pushchino. The space-weather and IPS data at Toyokawa and Pushchino for the period analyzed here are described in Sections 3, 4, and 5, respectively. The propagation profiles of halo CMEs derived from the IPS observations are presented in Section 6. We discuss and summarize the results obtained in Sections 7 and 8, respectively.

## 2. Observations

### 2.1. Toyokawa IPS Observations

IPS observations at 327 MHz have been conducted since the 1980s at the Toyokawa Observatory (longitude 133.37° E, latitude 34.83° N) of the Institute for Space-Earth Environmental Research (ISEE), the Nagoya University in Japan (Kojima and Kakinuma, 1990; Tokumaru, 2013). The IPS system currently used at Toyokawa is called the Solar Wind Imaging Facility Telescope (SWIFT: Tokumaru *et al.*, 2011). SWIFT is a meridian-transit-type radio telescope consisting of a cylindrical parabolic reflector with a size of 108 m (North–South)  $\times$  38 m (East–West) and a 192-element phased-array receiver that forms a single beam. The antenna beam is steerable between 60° South and 30° North in the zenith angle; *i.e.* -25° and 65° in the declination. SWIFT collects IPS data daily for 60–100 sources. Each IPS observation lasts about 200 second. The scintillation levels are derived from the power spectrum analysis of the SWIFT IPS data. The total fluctuation level, which includes both IPS and noise contributions, is determined for each observation by calculating the integral value of the power spectrum. The noise level is also determined from the power spectrum by detecting a flat portion at high frequencies, and subtracted from the total fluctuation level. The effect of the system-gain change is corrected by taking the ratio of the noise-subtracted level to the noise level. This ratio is used as the scintillation level. IPS observations at 327 MHz also have been made at Fuji and Kiso observatories simultaneously for the same sources as those observed at Toyokawa, although the number of sources observed at Fuji and Kiso are smaller than those at Toyokawa. The solar-wind speeds have been derived from the cross-correlation analysis of three-station IPS observations.

When wave scattering is weak, the scintillation level [ $I$ ] is related to the weighted integral value of  $\Delta N_e$  along the LOS through

$$I^2 \propto \int \Delta N_e^2 w(z) dz, \quad (1)$$

where  $w(z)$  is the IPS weighting function (Young, 1971; Tokumaru *et al.*, 2003),  $z$  is the distance along LOS. Since the  $\Delta N_e$  decreases as the distances from the Sun [ $R$ ] increases, the derived scintillation levels show the radial decrease with

$R$  of the LOS in the weak scattering region. For observations at 327 MHz, this relationship is valid when  $R > 0.2$  AU. To identify the CME signature (an abrupt jump in the scintillation level) efficiently, the  $g$ -values, which represents the daily variation of the scintillation level, i.e.  $\Delta N_e$  is calculated using the formula

$$g = \frac{I}{\overline{I(R)}}, \quad (2)$$

where  $I$  and  $\overline{I(R)}$  are the derived scintillation levels and the smoothed level given by the best-fit function  $aR^{-b}$  for  $R > 0.2$  AU (Tokumaru *et al.*, 2000). The smoothed level  $\overline{I(R)}$  is determined for each source on a yearly basis using all of the data for a given year. It includes not only the radial dependence of  $\Delta N_e$  but also the latitude dependence. When  $\Delta N_e$  is enhanced over the quiet level, we obtain  $g > 1$ . Note that all data with  $g > 1$  cannot be readily ascribed to the effect of CMEs, since they include the effect of the quasi-stationary structures of the solar wind such as corotating interaction regions. The value sufficiently greater than unity (e.g. 1.5) is used as a threshold level to identify IP disturbances associated with a CME (see Section 6). The  $g$ -values derived from Toyokawa IPS observations are available at <ftp.isee.nagoya-u.ac.jp/pub/vlist/>.

## 2.2. Pushchino IPS Observations

IPS observations with the upgraded large phased array called the Big Scanning Array (BSA) have been carried out since 2013 at the Pushchino Radio Astronomy Observatory (longitude 37.63° E, latitude 54.82° N) of the Lebedev Physical Institute in Russia. The observation frequency of the BSA is 111 MHz, and its aperture size is 384 m (North–South)  $\times$  187 m (East–West). The BSA is a meridian-transit type radio telescope, similarly to SWIFT, but it has 96 simultaneous beams. The multiple beams cover a declination range from  $-8^\circ$  to  $+42^\circ$ . Because of its extremely large aperture and multi-beam system, the BSA enables detection of IPS for more than 5000 sources a day, and then fine-resolution mapping of the solar wind (see Chashei *et al.*, 2015, 2016; Shishov *et al.*, 2016). The daily maps produced from Pushchino IPS observations are available at <astra.prao.psn.ru/c/SolarWeather.html>.

In this study, the  $g$ -value was derived from Pushchino IPS observations to make a combined analysis with Toyokawa IPS observations. We determined the scintillation level from Pushchino IPS observations for the radio sources observed at Toyokawa, and then we calculated the  $g$ -value using a method similar to that used for the Toyokawa observations. The smoothed scintillation level used for Pushchino  $g$ -value calculations was given by a linear function of time, since the analysis period for  $g$ -value; 1–15 September 2017, was too short to determine a reliable best-fit function of  $aR^{-b}$ . The inner limit distance of weak scattering was assumed to be 0.39 AU for 111 MHz. We derived 465  $g$ -values for 45 Toyokawa IPS sources from Pushchino data. The Pushchino  $g$ -value data derived here are available at <ftp.isee.nagoya-u.ac.jp/pub/vlist/>.

### 3. Space Weather During Early September 2017

Figure 1 shows the X-ray intensity and proton fluxes measured by the *Geostationary Operational Environmental Satellite* (GOES), and solar-wind density and speed measured by the *Solar Wind Electron Proton Alpha Monitor* (SWEPAM: McComas *et al.*, 1998) of the *Advanced Composition Explorer* (ACE) between 04 and 09 September 2017. Solar activity was raised significantly during this period owing to the emergence of the eruptive active region AR12673. This region produced a large number of solar flares including 4 X-class flares and 26 M-class flares between 04 and 10 September 2017. Among those flares, the M5.5/3B flare on 04 September 20:33 UT (SOL2017-09-04T20:33) and the X9.3/2B flare on 06 September 12:02 UT (SOL2017-09-06T12:02) caused enhancements in the  $> 10$  MeV proton flux at the geosynchronous orbit, which reached a maximum of 844 pfu on 08 September 00:35 UT. The locations of the M5.5 and X9.3 flares were S11W16 and S08W33, respectively. Another 10 MeV proton flux enhancements occurred in association with the X8.2 flare on 10 September (SOL2017-09-10T16:06), reaching a maximum of 1490 pfu.

Two full-halo CMEs were clearly recorded by the *Large Angle and Spectrometric COronagraph* (LASCO: Brueckner *et al.*, 1995) onboard the *Solar and Heliospheric Observatory* (SOHO) spacecraft, with one CME associated with the 04 September M5.5 flare (SOL2017-09-04T20:33) and the other associated with the 06 September X9.3 flare (SOL2017-09-06T12:02). Hereafter, these halo CMEs are called CME1 and CME2, the LASCO-C3 images of which are displayed in Figure 2a and b. The plane-of-sky (linear) speeds of CME1 and CME2 were 1420 and 1570 km s<sup>-1</sup>, respectively (from the SOHO/LASCO CME catalog, [cdaw.gsfc.nasa.gov/CME\\_list/](http://cdaw.gsfc.nasa.gov/CME_list/); Gopalswamy *et al.*, 2009). We note that higher plane-of-sky speeds were determined by the Computer Aided CME Tracking software package (CACTus: [sidc.oma.be/cactus/](http://sidc.oma.be/cactus/)): 1953 km s<sup>-1</sup> and 1955 km s<sup>-1</sup> for highest velocities of CME1 and CME2, respectively. During the period between 04 September 15:00 and 08 September 15:00, 15 CMEs were identified from LASCO observations (according to the SOHO/LASCO CME catalog), and there was neither other halo CME nor other CME with a plane-of-sky speed of  $> 1000$  km s<sup>-1</sup> than these two. Hence, CME1 and CME2 are considered as solar sources of observed IP disturbances. In earlier study (Chashei *et al.*, 2018), the CME associated with M3.2 flare on 05 September 4:53 UT (SOL2017-09-05T04:53), was assumed to be the cause for IP disturbances observed at Pushchino on 06 September. We consider that CME1 was more likely to cause the IP disturbances, since the 05 September CME had a small angular extent according to the CACTus (No report on this CME was found in the SOHO/LASCO CME catalog). LASCO observed another full-halo CME in association with the 10 September X8.2 flare; however, no associated IP shock was observed at Earth for this CME.

In-situ measurements by ACE showed the occurrence of IP shocks at the L<sub>1</sub> point on 06 September 23:08 UT and 07 September 22:54 UT. These two IP shocks (hereafter S1 and S2) are considered to correspond to CME1 and CME2, respectively. Solar wind speeds suddenly increased at both S1 and S2, with a rapid rise in the solar-wind density observed for S1, and a much less distinct

change in density for S2 (see Figure 1). The geomagnetic field was significantly disturbed after the arrival of these shocks, particularly when the interplanetary magnetic field (IMF) Bz component was directed southward. A sudden storm commencements (ssc) were observed at the Kakioka Magnetic Observatory on 06 September 23:44 UT and 07 September 23:00 UT, and the Dst-index during the geomagnetic storms reached a minimum value of -124 nT on 08 September 02:00 UT.

#### 4. Toyokawa IPS Maps

Figures 3a–d show the Toyokawa  $g$ -value maps between 04 and 08 September. In these maps, the  $g$ -values are plotted in the sky plane centered at the Sun on a daily basis. The solid circles indicate the plane-of-sky locations of the LOS for the sources, with their color and size representing the strength of the  $g$ -value. The dotted circles are constant distance contours, and the innermost circle corresponds to 0.2 AU, which is the inner-boundary distance for  $g$ -value measurements at 327 MHz. The  $g$ -value map of 04–05 September shows that the inner solar wind was mostly quiet, *i.e.* no systematic enhancement in the  $g$ -value was found (Figure 3 a). In contrast, marked enhancements were observed in the  $g$ -value maps on the following three days (see Figures 3b–d). These  $g$ -value enhancements are considered IP disturbances caused by the halo CMEs.

Figure 3b shows intense  $g$ -value enhancements between 05 and 06 September at about 0.8 AU west near the Equator. The center of the IP disturbances was found to be located near the Sun–Earth line, but shifted slightly west, considering the IPS weighting function for the plane-of-sky distance of 0.8 AU. These locations are generally consistent with the LASCO image of CME1, and their observation times are consistent with the arrival time of S1. The intense  $g$ -value enhancements observed between 06 and 07 September were located in the West–South quadrant at about 0.5 AU (see Figure 3c). These locations and observation times agree with the LASCO image of CME2 and the arrival time of S2. Thus, the  $g$ -value enhancements are considered to represent IP shocks driven by the halo CMEs. Note that the transit speeds inferred from the plane-of-sky locations of the  $g$ -value enhancements for 05–06 and 06–07 September are significantly higher than those of the IP shocks derived from the arrival time at 1 AU. This difference may be ascribed to the deceleration of IP shocks during propagation. We address the propagation profile of the CME-associated shocks in more detail in Section 6. Another interesting feature to note is the arc-shaped  $g$ -value enhancements seen in the IPS map between 07 and 08 September (see Figure 3d). This feature was observed prominently in the East–North quadrant which is the opposite quadrant where the  $g$ -value enhancements associated with CME2 were observed on the previous day. Moreover, the observation time of these  $g$ -value enhancements was later than the arrival time of S2 at Earth. Further discussion on the origin of these  $g$ -value enhancements is presented in Section 7.1. The  $g$ -value map for 08–09 September (not shown in the figure) indicates that the inner solar wind returned to the quiet state. The total number of  $g$ -value enhancements with  $g > 1.5$  ( $g > 2$ ) was 50 (25) between 04 September

18:00 UT and 08 September 11:00 UT. These enhancements are much greater than fluctuations caused by the error of  $g$ -value measurements, and also greater than those caused by quasi-stationary structures of the solar wind (see Section 6).

The sky-projection maps of the solar-wind speed derived from ISEE IPS observations between 04 and 08 September are shown in Figure 3e–h. The format of these maps are the same as that of the  $g$ -value maps (Figure 3a–d). While the number of LOS for the speed map was smaller than the  $g$ -value map, extremely high ( $> 1000 \text{ km s}^{-1}$ ) speed streams were found in the maps of 05–06 and 06–07 September. There was no one-to-one correspondence between locations of those high-speed data and high  $g$ -value data, and the high-speed streams appear to be located closer to the Sun, compared to the  $g$ -value enhancements. This fact may be ascribed to different distributions of the IP shock and the driving flow, although the number of the data is too small to conclude. Further discussion on the speed data is left to a future study, and hereafter we devote ourselves to comparing the  $g$ -value data from Toyokawa IPS observations with Pushchino data.

## 5. Pushchino IPS Maps

Enhancements of IPS strength are also identified in the  $g$ -value data derived from the Pushchino IPS observations. Figures 3i–l show the Pushchino  $g$ -value maps between 05 and 09 September. The  $g$ -values are indicated in the sky projection map by circles, similarly to the Toyokawa IPS maps. The Pushchino  $g$ -value data are available only for distances  $> 0.39 \text{ AU}$  (the weak scattering region). Many  $g$ -value enhancements occurred, particularly at nighttime when ionospheric scintillation effects become significant, and those observed at distances  $> 1 \text{ AU}$  (nighttime data) were ignored in this study. This greatly reduced the number of valid  $g$ -value enhancements. The reason why the number of daytime  $g$ -value data is so limited is that the radio sources used in this study were optimized for ISEE IPS observations, not for Pushchino IPS observations with their different frequencies and different geographic latitudes. The use of the source list optimized for the Pushchino observations would have improved the IPS maps, although it was beyond the scope of this article. Nevertheless,  $g$ -value enhancements with  $g > 1.5$  ( $g > 2$ ) were identified for 19 (7) LOS between 0.39 and 1 AU in the analysis period. The  $g$ -value enhancements were observed mostly in the northeast quadrant at  $\approx 0.9 \text{ AU}$  on 07 September (Figure 3k), and in the west at  $\approx 0.8 \text{ AU}$  on 08 September (Figure 3l). These enhancements may represent IP disturbances associated with the halo CMEs, as discussed in the next section.

## 6. Propagation of the Halo CMEs in the Solar Wind

Figure 4 presents a plot of the observation times versus the plane-of-sky distances  $R$  for  $g > 1.5$  identified from the Toyokawa and the Pushchino observations from 05 to 08 September. The threshold value (1.5)

approximately corresponds to the mean plus one  $\sigma$  of ISEE  $g$ -value data, and was used for identification of IP disturbances in our earlier studies (Tokumaru *et al.*, 2000; Iju, Tokumaru and Fujiki, 2013). The  $g$ -value variations within one  $\sigma$  include contributions from quasi-stationary solar-wind structures such as corotating interaction regions, and to a lesser extent the measurement error. The  $g$ -value enhancements with  $g > 1.5$  are mostly ascribed to significant IP disturbances. The data with  $g > 2$ , which are indicated by larger symbols in the figure, correspond to more prominent disturbances whose identifications have a better confidence level than those of  $2 > g > 1.5$ . We note that the identification of IP disturbances from Pushchino  $g$ -value data may not be as reliable as that from Toyokawa data, since the period used to determine the smoothed level was short. The constant speed propagation lines of IP shocks associated with CME1 and CME2; *i.e.* S1 and S2, are indicated in this figure. The average transit speeds of S1 and S2 at 1 AU were 790 and 1190 km s<sup>-1</sup>, respectively. The constant-speed propagation lines with a plane-of-sky speed measured by LASCO are also indicated for CME1 and CME2 in the figure.

The plane-of-sky locations of  $g$ -value enhancements are influenced by the LOS integration effect, sometimes significantly. The bias caused by the LOS integration effect depends on several factors such as the propagation direction and angular extent of the IP disturbances, anisotropy of expansion, and the radial distance where IPS observations are made. For an Earth-directed event, the most severe bias should occur at small distances, and the plane-of-sky location tends to underestimate the actual radial distance as the angular extent decreases (Tokumaru *et al.*, 2005). Nevertheless, the plane-of-sky location of  $g$ -value enhancements is not much different from the actual location if the angular extent of the high- $\Delta N_e$  region is sufficiently wide (Tokumaru *et al.*, 2005). Since CME1 and CME2 were associated with intense solar flares, resultant IP disturbances are considered large-scale. Therefore, we considered that the LOS integration effect did not bias the IPS data significantly, and we analyzed only the plane-of-sky locations of  $g$ -value enhancements in this study. We note that the LOS integration effect tends to increase the radial width of IP disturbances in the sky projection map, when the spatial distribution deviates from spherical symmetry.

The following points are revealed from Figure 4:

- i) The  $g$ -value enhancements observed between 04 September 18:00 UT and 05 September 11:00 UT from Toyokawa observations are considered to represent IP disturbances excited by solar activity before CME1, although no coronal counterpart was reported from LASCO observations of the preceding one or two days. We ignored them in the present study. Some transient high-speed streams were found in the East of the speed map for 04–05 September (Figure 3e), and this may be regarded as an observational evidence to support the occurrence of the preceding IP disturbances.
- ii) The  $g$ -value enhancements were detected for many LOS between 05 September 18:00 UT and 06 September 11:00 UT from Toyokawa observations, while no  $g$ -value with  $g > 1.5$  was available at Pushchino for this time interval. These disturbances are ascribed mostly to the IP shock associated with CME1. The majority of the Toyokawa data are above the constant-speed propagation

line of the IP shock, suggesting a propagation speed higher than the average transit speed of S1 ( $790 \text{ km s}^{-1}$ ), as mentioned in Section 4. Some  $g$ -value data for 05–06 September may be ascribed to another origin. The  $g$ -value data near 0.2 AU is likely to represent the effect of different CMEs, and hence were not included in the analysis of either CME1 or CME2. Those observed near 1 AU on 05 September at  $\approx 22:00$  UT might correspond to the preceding IP disturbances, but they were included in the analysis of CME1, since they are close to the constant-speed propagation line of CME1 with a plane-of-sky speed measured by LASCO.

- iii) Many  $g$ -value enhancements were observed at both Toyokawa and Pushchino for the periods between 06 September 18:00 UT–07 September 11:00 UT and between 07 September 00:00–17:00 UT, respectively. The important point is that the  $g$ -value enhancements were observed at Pushchino several hours later than at Toyokawa. This fact means that the temporal cadence in tracking the CME-driven IP shock was improved by combining these data. While the  $g$ -value data from Toyokawa observations are distributed broadly between 0.2 and 1 AU, the majority of the data, particularly those with  $g > 2$ , are above the constant-speed propagation line of the IP shock. The  $g$ -value data from Pushchino observations show a similar tendency. This fact suggests that the IP shock near the Sun propagated at a speed higher than the average shock-transit speed. The data near 1 AU on 06 September  $\approx 22:00$  UT may be attributed to the IP shock associated with CME1. Some of  $g$ -value data are located below the constant-speed propagation line. These data may represent either a highly warped complex structure of the IP shock or an internal structure of disturbances associated with CME2 (see below).
- iv) The  $g$ -value enhancements were obtained again from both Toyokawa (07 September 18:00 UT–08 September 11:00 UT) and Pushchino (07 September 00:00–17:00 UT) observations almost simultaneously for different LOS. The radial distances of those  $g$ -value enhancements are generally consistent with each other, although  $g$ -value data taken at Toyokawa on 08 September 00:00–02:00 UT show a large spread of the locations. Note that  $g$ -value enhancements were observed prominently on the East side of the Sun at Toyokawa, whereas they were observed on the West at Pushchino. Those data appear inconsistent with the IP shock S2, and they suggest a transit speed much slower than that of IP shock S2, as discussed below. The  $g$ -value data taken near 0.2 AU on 08 September were ignored in the analysis of CME2, since they are considered as the effect of different CMEs.

Thus, the  $g$ -value data at Toyokawa are generally consistent with those at Pushchino, especially when focusing on those with  $g > 2$ . They suggest that the IP shocks were significantly decelerated during propagation between the Sun and the Earth orbit. In this study, we derived the deceleration profile of the IP shocks by combining between LASCO, IPS, and ACE data. The method used here is basically the same as the one used by Iju, Tokumaru, and Fujiki (2013, 2014); we calculated average transit speeds of the IP shocks for two distance ranges, namely, the one from LASCO and IPS data and the other from IPS and ACE data. In calculating the average transit speeds, we ignored the data taken before

05 September 08:00 UT, and also those taken near 0.2 AU. The deceleration profiles using the average transit speeds are shown in Figure 6 (dot-dashed lines), and it can be regarded as the first-order approximation of the actual deceleration profile. It should be noted that spherically symmetric expansion of the IP shocks is assumed in this analysis. As shown in the figure, the deceleration of CME2 is modest compared to that of CME1. This fact may be ascribed to the sweeping effect by CME1.

The expansion speed of the IP shock may depend on the separation angle to the disturbance center located above the eruption site. We investigated the angular dependence of the propagation speeds of the IP shocks using Toyokawa and Pushchino  $g$ -value data. We calculated the daily mean values of Toyokawa and Pushchino  $g$ -value data for the period between CME and IP shock occurrence times of each event, and we plotted them in a time-distance diagram for CME1 and CME2 events, with separate mean values for data on the east and west sides of the Sun. Although the  $g$ -value data more or less contain the LOS integration effect, it is possible to address the East-West asymmetry of the propagation speed of IP shocks by comparing between the mean values. The ensemble average of the distances [ $R$ ] is considered to give a better estimate of the actual location of IP disturbances, since the distances [ $R$ ] of  $g$ -value data shown in Figure 4 are determined by the observation time, and they do not necessarily represent the peak location of IP disturbances. Here, we note that the contamination by data associated with the different CME may arise between the CME2 occurrence time (06 September 12:00 UT) and the S1 IP shock arrival (06 September 23:00 UT).

Figure 5 shows the time-distance plot for the CME1 event, and it includes the Toyokawa  $g$ -value data with  $g > 1.5$ , the constant-speed propagation line derived from the occurrence time of S1 and that estimated from the plane-of-sky distance of  $g$ -value enhancements. The  $g$ -value data on the West side for 06 September suggests a propagation speed faster than those on the East. The average propagation speed derived from all  $g$ -value data for September 6 was  $1008 \text{ km s}^{-1}$ . Since there are more  $g$ -value data from the West than from the East, the dot-dashed line that indicates the constant-speed propagation of the IPS shock inferred from the  $g$ -value data is closer to the West-side data. As shown in the figure, the  $g$ -value data suggest that the propagation speed of S1 in the inner solar wind was significantly faster than the average transit speed, implying that it rapidly decelerated during propagation. The Toyokawa  $g$ -value data on the east side were also available for 07 September in this interval. The average speed derived from this data was  $637 \text{ km s}^{-1}$ , slower than the average transit speed of S1. The slower speed may be attributed to the contamination effect by CME2 data.

Figure 6 shows the time-distance plot of the  $g$ -value data for the CME2 event. This plot includes  $g$ -value data with  $g > 1.5$  of Toyokawa and Pushchino for September 8, the constant speed propagation line of the IP shock S2 ( $1190 \text{ km s}^{-1}$ ), and those inferred from the  $g$ -value data. The average transit speeds are determined from Toyokawa and Pushchino data separately for each day. As shown here, the  $g$ -value data at Toyokawa and Pushchino are quite consistent with the constant-speed propagation line for both east and west sides. The speeds from

the Toyokawa and Pushchino data for 07 September were 1937 and 1324 km s<sup>-1</sup>, respectively, much higher than the average transit speed of S2. Similar to the case of CME1, hence the  $g$ -value data suggest that the IP shock with a very fast initial speed decelerated as it propagate through the solar wind. The important point to note here is that the temporal cadence for tracking the IP shock was improved by combining IPS observations taken at Toyokawa and Pushchino. The slower average speed from Pushchino observations, compared to that from Toyokawa, may be ascribed to the deceleration effect. The  $g$ -value data observed on the West at Toyokawa for 07 September  $\approx$ 00:00 UT may be influenced by the contamination by CME1 data. However, we consider that the data are not influenced seriously by that effect, since the data are consistent with those from Pushchino observations. Another important point is that the  $g$ -value data observed on the West side indicated systematically higher speeds than those on the East side, and this is similar to the case of CME1. The difference may be due to angular dependence of the CME expansion speed. This interpretation is consistent with the fact that the sites of associated flares were located on the West side with respect to the Sun–Earth line. In contrast, the average transit speeds derived from the  $g$ -value data of 08 September were 677 and 755 km s<sup>-1</sup> for Toyokawa and Pushchino, respectively, much slower than the average transit speed of S2 (1190 km s<sup>-1</sup>). Hereafter, we call this the slow disturbance, and we address its origin in Section 7.1. Since the transit speed derived from Toyokawa data is similar to that from Pushchino data, the slow disturbance appeared to expand nearly uniformly in longitude. These transit speeds were also close to the ambient solar-wind speed (600–700 km s<sup>-1</sup>).

## 7. Discussion

### 7.1. Origin of the Slow Disturbance

The slow disturbance was considered as an interplanetary consequence of CME2, since no other halo CME was observed in the analysis period. One possible origin for the slow disturbance observed on 07–08 September is the wing part of the IP shock driven by CME2. According to this interpretation, the wing part of the IP shock must be extremely extended in longitude from the eruption site, and the expansion speed of the IP shock must have a marked angular dependence with the wing part moving about two times slower than the central part. This interpretation was generally consistent with the angular dependence of the shock expansion speed revealed from the analysis for CME2. Another possible origin is a dense plasma confined within CME2. As mentioned before, the internal region of a CME observed in the interplanetary space is usually associated with a rarefied plasma, and no distinct density increase was observed after the shock passage from in situ measurements for CME2 (*e.g.* Figure 1 of Shen *et al.*, 2018). Nevertheless, we cannot safely rule out this possibility, since an internal structure with a high density which is remotely located from the Earth may give rise to  $g$ -value enhancements. To account for the observed data, this structure must significantly extend to both East and West sides, and it should not encounter the

Earth. Since many CMEs occurred and propagated into the existing corotating streams during the analysis period, a complex structure may be formed through the interaction between CMEs and the solar wind (Shen *et al.*, 2018). It is difficult to distinguish between these two possibilities in this study, and hence the origin of the slow disturbance remains unsettled.

## 7.2. LOS Integration Effect and Global Feature of IP Shocks

As mentioned in Section 6, we ignore the LOS integration effect in this study, and the plane-of-sky location of  $g$ -value enhancements tends to underestimate the actual distance of the IP shock by this effect when the angular extent becomes small. Therefore, the actual deceleration of the IP shocks would be more rapid than that inferred from the plane-of-sky locations of  $g$ -value data if the events had a small angular extent. The deconvolution analysis of IPS observations such as the time-dependent tomography (Jackson *et al.*, 2011) or the model fitting method (Tokumaru *et al.*, 2003) is useful for eliminating a bias due to the LOS integration effect and reconstructing the 3D distribution of CMEs in the solar wind, and it may provide an improved view of the propagation of the IP shocks in the inner heliosphere and the interaction between CMEs and the solar wind, while it is beyond the scope of this article.

## 8. Summary

IPS observations at Toyokawa and Pushchino in early September 2017 were analyzed to investigate the propagation of halo CMEs in the interplanetary space. The results obtained from this analysis are summarized as follows:

- i) The  $g$ -value enhancements, which corresponded to the IP shocks driven by halo CMEs on 04 and 06 September (CME1 and CME2), were detected from IPS observations at Toyokawa. The IP shocks driven by CME2 was also detected from IPS observations at Pushchino, and the plane-of-sky locations of the  $g$ -value enhancements at both sites were consistent with each other. The time–distance plots derived from the  $g$ -value data for CME1 and CME2 suggested that the IP shocks between the Sun and the Earth’s orbit rapidly decelerated, and also that the propagation speeds of the IP shocks on the west side were significantly faster than those on the east side.
- ii) The  $g$ -value enhancements observed at both sites on 07–08 September suggest that the IP disturbance propagated at a speed significantly slower than the average transit speed of the CME2-driven IP shock. This slow disturbance may be ascribed either the wind part of the CME2-driven shock with marked longitude dependence of the expansion speed or the internal high-density structure within CME2, while further discussion on it is deferred to future study.

As demonstrated in this study, the world-wide network of IPS observations, *i.e.* WIPSS, enables detection and tracking of fast-moving CMEs with an improved temporal cadence. Tomographic analysis, which provides an unbiased view of the global solar wind from IPS observations, helps optimize the utility of WIPSS for space weather predictions, and therefore it is a promising future study.

**Acknowledgments** The IPS observations at Toyokawa were conducted under the solar-wind program of the Institute for Space-Earth Environmental Research (ISEE). We thank the SOHO Science Archive ([sohowww.nascom.nasa.gov/](http://sohowww.nascom.nasa.gov/)), the National Centers for Environmental Information ([satdat.ngdc.noaa.gov/](http://satdat.ngdc.noaa.gov/)), and the ACE Science Center ([www.srl.caltech.edu/ACE/ASC/](http://www.srl.caltech.edu/ACE/ASC/)) for providing the LASCO, GOES, and ACE data, respectively. The information on the geomagnetic storms was obtained from the Kakioka Magnetic Observatory website ([www.kakioka-jma.go.jp/](http://www.kakioka-jma.go.jp/)). This CME catalog is generated and maintained at the CDAW Data Center by NASA and The Catholic University of America in cooperation with the Naval Research Laboratory. SOHO is a project of international cooperation between ESA and NASA. This article uses data from the CACTus CME catalog, generated and maintained by the SIDC at the Royal Observatory of Belgium. S. Tyul'bashev and I. Chashei are grateful to I.A. Subaev for assistance in preparation of the Pushchino data.

**Disclosure of Potential Conflicts of Interest** The authors declare that they have no conflicts of interest.

## References

- Armstrong, J.W., Coles, W.A.: 1978, Interplanetary scintillation of PSR 0531+21 at 74 MHz, *Astrophys. J.* **220**, 346. DOI.
- Bisi, M.M., Gonzalez-Esparza, A., Jackson, B.V., Aguilar-Rodriguez, E., Tokumaru, M., Chashei, I.V., Tyul'bashev, S.A., Manoharan, P.K., Fallows, R.A., Chang, O., Mejia-Ambriz, J.C., Yu, H.S., Fujiki, K., Shishov, V.: 2016, The Worldwide Interplanetary Scintillation (IPS) Stations (WIPSS) Network in Support of Space-Weather Science and Forecasting, *Am Geophys Un, Fall Gen Ass* abstract id. PA41A-2135.
- Brueckner, G.E., Howard, R.A., Koomen, M.J., Korendyke, C.M., Michels, D.J., Moses, J.D., Socker, D.G., Dere, K.P., Lamy, P.L., Llebaria, A., Bout, M.V., Schwenn, R., Simnett, G.M., Bedford, D.K., Eyles, C.J.: 1995, The Large Angle Spectroscopic Coronagraph (LASCO), *Solar Phys.* **162**, 357. ADS, DOI.
- Chashei, I.V., Shishov, V.I., Tyulbashev, S.A., Subaev, I.A., Oreshko, V.V., Logvinenko, S.V.: 2015, Global structure of the turbulent solar wind during 24 solar activity maxima from IPS observations with the multibeam radio telescope BSA LPI at 111 MHz, *Solar Phys.* **290**, 2577. ADS, DOI.
- Chashei, I.V., Tyul'bashev, S.A., Shishov, V.I., Subaev, I.A.: 2016, Interplanetary and ionosphere scintillation produced by ICME 20 December 2015, *Space Weather* **14**, 682 DOI.
- Chashei, I.V., Tyul'bashev, S.A., Shishov, V.I., Subaev, I.A.: 2018, Coronal mass ejections in September 2017 from monitoring of interplanetary scintillations with the Large Phased Array of the Lebedev Institute of Physics, *Astron. Rep.* **62**, 346. DOI.
- Coles, W.A., Harmon, J.K., Lazarus, A.J., Sullivan, J.D.: 1978, Comparison of 74 MHz interplanetary scintillation and IMP 7 observations of the solar wind during 1973, *J. Geophys. Res.* **83**, 3337. DOI.
- Gopalswamy, N., Yashiro, S., Michalek, G., Stenborg, G., Vourlidas, A., Freeland, S., Howard, R.: 2009, The SOHO/LASCO CME Catalog, *Earth, Moon, and Planets* **104**, 295. DOI
- Hewish, A., Scott, P.F., Wills, D.: 1964, Interplanetary scintillation of small diameter radio sources, *Nature* **203**, 1214. DOI.
- Iju, T., Tokumaru, M., Fujiki, K.: 2013, Radial speed evolution of interplanetary coronal mass ejections during solar cycle 23, *Solar Phys.* **288**, 331. ADS, DOI.
- Iju, T., Tokumaru, M., Fujiki, K.: 2014, Kinematic propagation of slow ICMEs and an interpretation of a modified drag equation for fast and moderate ICMEs, *Solar Phys.* **289**, 2157. DOI.
- Jackson, B.V., Hick, P.P., Buffington, A., Bisi, M.M., Clover, J.M., Tokumaru, M., Fujiki, K.: 2011, Three-dimensional reconstruction of heliospheric structure using iterative tomography: A review, *J. Atmos., Sol. Terr. Phys.* **73**, 1214. DOI.

- Kojima, M., Kakinuma, T.: 1990, Solar cycle dependence of global distribution of solar wind speed, *Space Sci. Rev.* **53**, 173. DOI.
- Lynch, B.J., Coles, W.A., Sheeley, N.R.: 2002, A comparison of mean density and microscale density fluctuations in a CME at 10  $R_S$ , *Geophys. Res. Lett.* **29**, 1913. DOI.
- Manoharan, P.K.: 2006, Evolution of coronal mass ejections in the inner heliosphere: a study using white-light and scintillation images, *Solar Phys.* **235**, 345. ADS, DOI.
- Manoharan, P.K., Tokumaru, M., Pick, M., Subramanian, P., Ipavich, F.M., Schenk, K., Kaiser, M.L., Lepping, R.P., Vourlidas, A.: 2001, Coronal mass ejection of July 14, 2000 Flare Event: Imaging from near-Sun to Earth environment, *Astrophys. J.* **559**, 1180. DOI.
- McComas, D.J., Bame, S.J., Barker, P., Feldman, W.C., Phillips, J.L., Riley, P., Griffee, J.W.: 1998, Solar Wind Electron Proton Alpha Monitor (SWEPAM) for the Advanced Composition Explorer, *Space Sci. Rev.* **86**, 563. DOI.
- Moore, V., Harrison, R.A.: 1994, A characterization of discrete solar wind events detected by interplanetary scintillation mapping, *J. Geophys. Res.* **99**, 27. DOI.
- Shen, C., Xu, M., Wang, Y., Chi, Y., and Luo, B.: 2018, Why the shock-ICME complex structure is important: learning from the early 2017 September CMEs, *Astrophys. J.* **861**, 28. DOI.
- Shishov, V.I., Vlasov, V.I., Kojima, M.: 1997, Structure of interplanetary shock waves from radio scintillation data, *Solar Phys.* **176**, 373. ADS, DOI.
- Shishov, V.I., Chashei, I.V., Oreshko, V.V., Logvinenko, S.V., Tyul'bashev, S.A., Subaev, I.A., Svidskii, P.M., Lapshin, V.M., Dagkesamanskii, R.D.: 2016, Monitoring of the turbulent solar wind with the upgraded Large Phased Array of the Lebedev Institute of Physics: First results, *Astron. Rep.* **12**, 1067. DOI.
- Tokumaru, M.: 2013, Three-dimensional exploration of the solar wind using observations of interplanetary scintillation, *Proc. Japan. Acad., Ser. B* **89**, 67. DOI.
- Tokumaru, M., Kojima, M., Fujiki, K., Yokobe, A.: 2000, Three-dimensional propagation of interplanetary disturbances detected with radio scintillation measurements at 327 MHz, *J. Geophys. Res.* **105**, 10435. DOI.
- Tokumaru, M., Kojima, M., Fujiki, K., Yamashita, M., Yokobe, A.: 2003, Toroidal-shaped interplanetary disturbance associated with the halo coronal mass ejection event on July 14, 2000, *J. Geophys. Res.* **108**, 1220. DOI.
- Tokumaru, M., Kojima, M., Fujiki, K., Yamashita, M., Baba, D.: 2005, Interplanetary consequences caused by the extremely intense solar activity during October–November 2003, *J. Geophys. Res.* **110** A01109. DOI.
- Tokumaru, M., Kojima, M., Fujiki, K., Yamashita, M., 2006, Tracking heliospheric disturbances by interplanetary scintillation, *Nonlin. Proc. Geophys.* **13**, 329. DOI.
- Tokumaru, M., Kojima, M., Fujiki, K., Yamashita, M., Jackson, B.V.: 2007, The source and propagation of the interplanetary disturbance associated with the full-halo coronal mass ejection on October 28, 2003, *J. Geophys. Res.* **112**, A05106. DOI.
- Tokumaru, M., Kojima, M., Fujiki, K., Maruyama, M., Maruyama, Y., Ito, H., Iju, T.: 2011, A newly-developed UHF radiotelescope for interplanetary scintillation observations; Solar Wind Imaging Facility, *Radio Sci.* **46**, RS0F02. DOI.
- Vlasov, V.I.: 1979, Radio imagery of the turbulent interplanetary plasma, *Sov. Astron.* **3**, 55. ADS.
- Young, A. T.: 1971, Interpretation of interplanetary scintillation, *Astrophys. J.* **168**, 543. DOI.

2017/09/04:15.0UT–2017/09/09:15.0UT

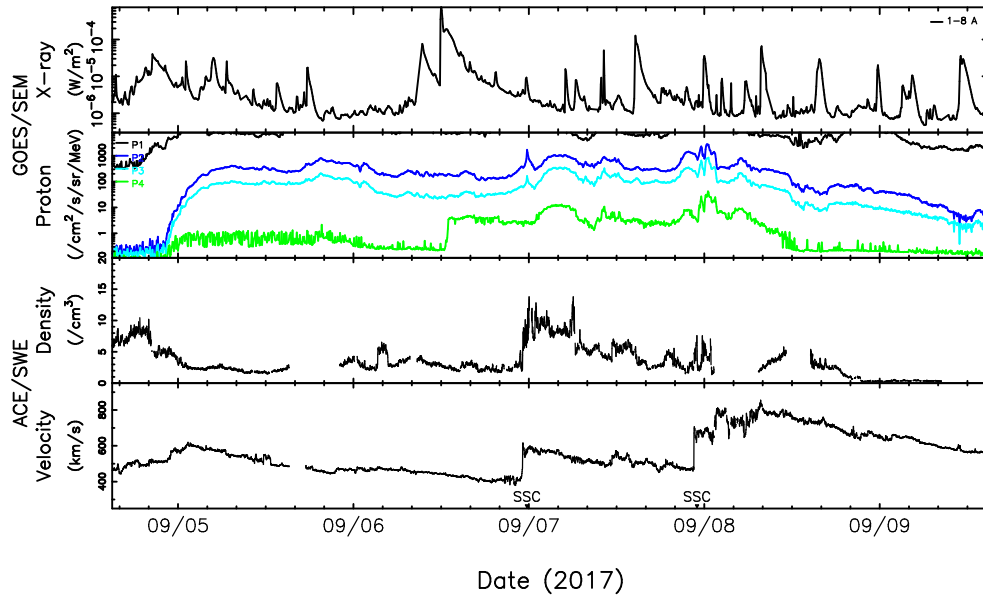


**Figure 1.** Space weather from 04 September 2017 15:00 to 09 September 2017 15:00. (From **top to bottom**) Solar soft (1–8 Å) X-ray flux and energetic (P1: 0.7–4 MeV, P2: 4–9 MeV, P3: 9–15 MeV, P4: 15–40 MeV) proton flux measured by GOES, solar-wind density and speed measured by SWEPAM/ACE, respectively. In the bottom panel, the occurrence times of sudden storm commencements (ssc) are indicated by triangles on the x-axis.

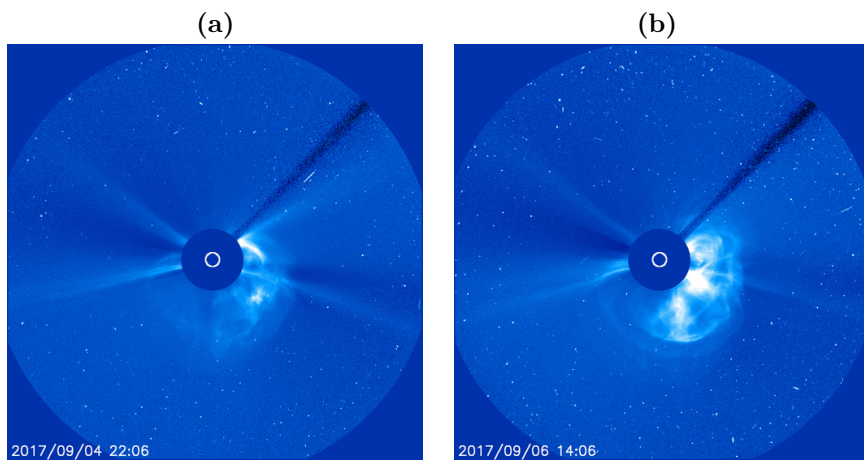


**Figure 2.** LASCO-C3 images of (a) CME1 and (b) CME2.

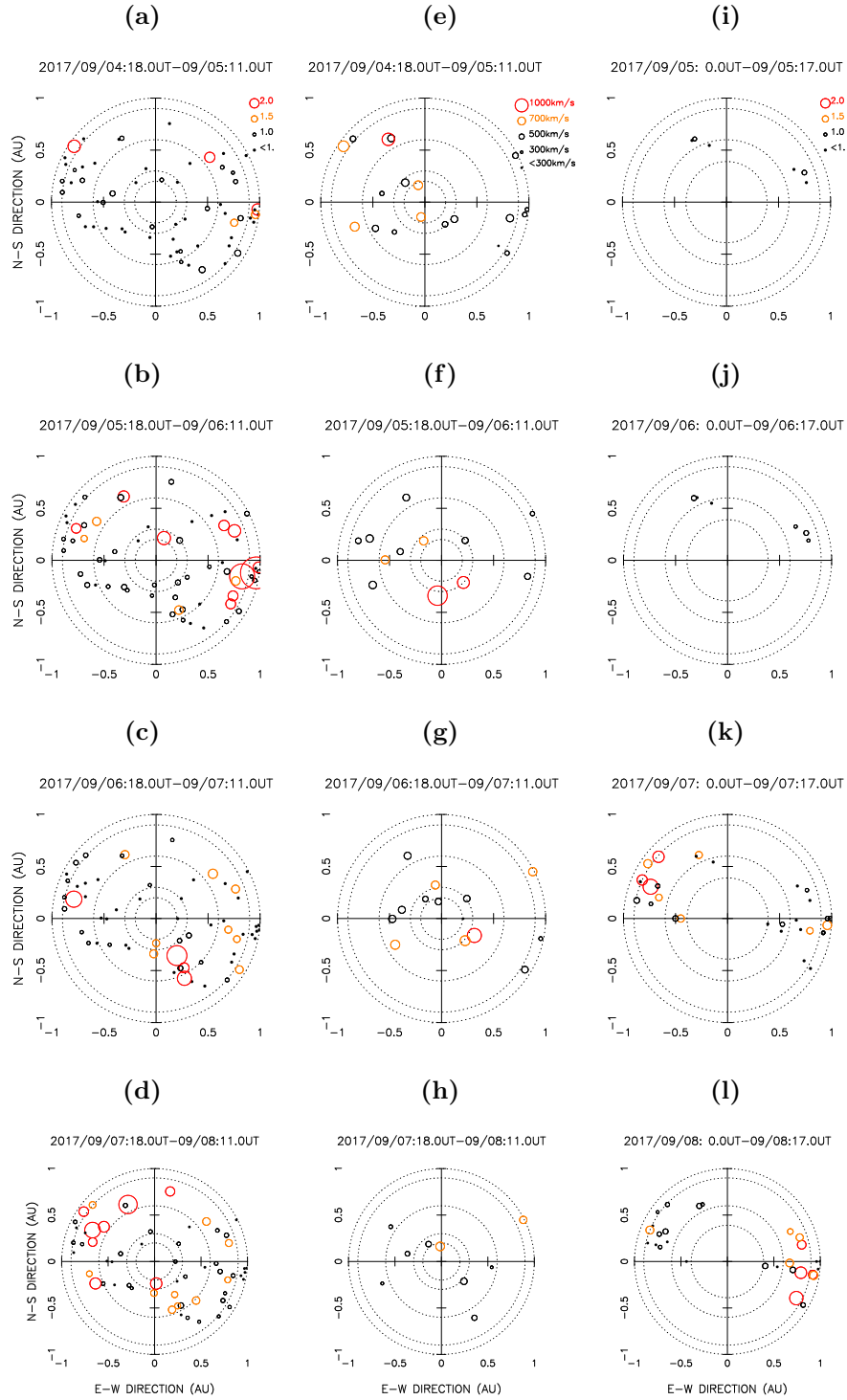


**Figure 3.** Sky projection maps of (**left column**)  $g$ -values and (**middle column**) solar-wind speeds derived from Toyokawa IPS observations, and (**right column**)  $g$ -values derived from Pushchino observations for 04–05 (**a, e, i**), 05–06 (**b, f, j**), 06–07 (**c, g, k**), and 07–08 (**d, h, l**) September 2017. Solid circles in these maps indicate the plane-of-sky locations of the LOS for the sources, and their color and size represent either the  $g$ -value strength or the speed. Dotted circles are contours of constant distance from the Sun, and the innermost circles of the Toyokawa and Pushchino maps correspond to 0.2 and 0.39 AU, respectively (the inner limit distance of weak scattering for either 327 MHz or 111 MHz).

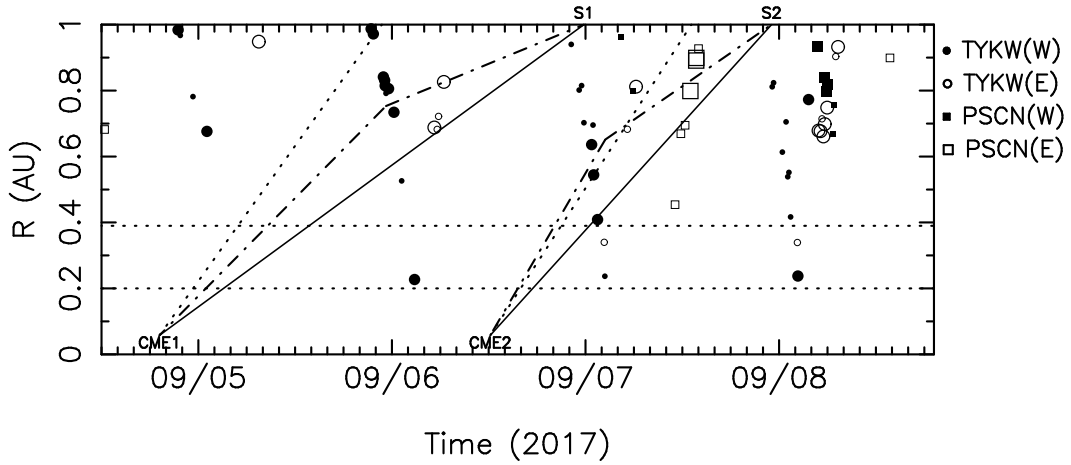


**Figure 4.** Time–distance plot of IP disturbances identified from Toyokawa and Pushchino IPS observations between 04 and 08 September 2017. Open and solid circles denote  $g$ -value enhancements ( $g > 1.5$ ) from Toyokawa IPS observations, and open and solid squares denote those from Pushchino IPS observations. Open and solid symbols correspond to data taken on the East and the West sides of the Sun. Larger symbols denote  $g > 2$ . The horizontal dotted lines indicate the inner boundary distances for the Pushchino (**upper**) and Toyokawa (**lower**) IPS measurements. The solid oblique lines correspond to the constant-speed propagation of IP shocks associated with CME1 and CME2; *i.e.* S1 and S2. The dotted oblique lines correspond to the constant-speed propagation of CMEs with plane-of-sky speeds derived LASCOS observations. The dot-dashed lines represent the deceleration profiles approximated by two constant speeds derived from LASCOS, IPS, and ACE data.

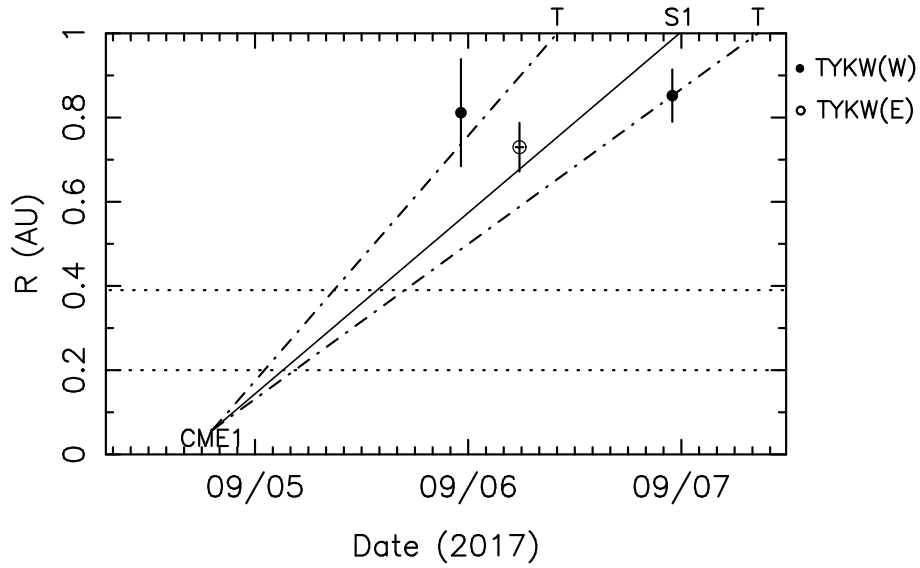


**Figure 5.** Time–distance plot of the IP disturbances associated with CME1. Open and solid circles indicate the daily mean plane-of-sky distances of the Toyokawa  $g$ -value enhancements observed for the East and West sides of the Sun, respectively. The solid line corresponds to the constant-speed propagation of the IP shock S1 derived from the occurrence time. The dot-dashed line corresponds to the constant-speed propagation of the IP shock inferred from the  $g$ -value data. The horizontal dotted lines indicate the inner-boundary distances for the Pushchino (**upper**) and Toyokawa (**lower**) IPS measurements.

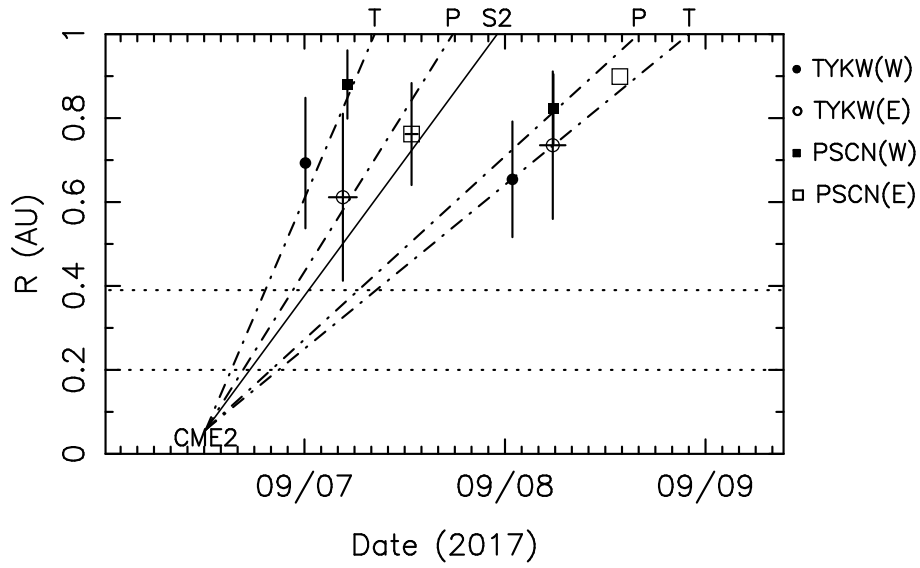


**Figure 6.** Time–distance plot of the IP disturbances associated with CME2. Circles and squares represent Toyokawa and Pushchino  $g$ -value data, respectively. Open and solid symbols are the data of the East and the West sides of the Sun, respectively. The solid line corresponds to the constant-speed propagation of the IP shock S2. The dot-dashed lines correspond to the constant-speed propagation of the IP shock inferred from the Toyokawa (T) and Pushchino (P)  $g$ -value data. The horizontal dotted lines indicate the inner-boundary distances for the Pushchino (**upper**) and Toyokawa (**lower**) IPS measurements.